Optics Letters

# High-performance and linear thin-film lithium niobate Mach–Zehnder modulators on silicon up to 50 GHz

Ashutosh Rao,[1] Aniket Patil,[2] Payam Rabiei,[2] Amirmahdi Honardoost,[1] Richard DeSalvo,[3] Arthur Paolella,[3] and Sasan Fathpour[1,4,*]

[1]CREOL, College of Optics and Photonics, University of Central Florida, Orlando, Florida 32816, USA
[2]Partow Technologies LLC, Orlando, Florida 32816, USA
[3]Harris Corporation, Melbourne, Florida 32901, USA
[4]Department of Electrical and Computer Engineering, University of Central Florida, Orlando, Florida 32816, USA
*Corresponding author: fathpour@creol.ucf.edu

Received 17 October 2016; revised 11 November 2016; accepted 15 November 2016; posted 15 November 2016 (Doc. ID 278541); published 7 December 2016

**Compact electro-optical modulators are demonstrated on thin films of lithium niobate on silicon operating up to 50 GHz. The half-wave voltage length product of the high-performance devices is 3.1 V.cm at DC and less than 6.5 V.cm up to 50 GHz. The 3 dB electrical bandwidth is 33 GHz, with an 18 dB extinction ratio. The third-order intermodulation distortion spurious free dynamic range is 97.3 dBHz$^{2/3}$ at 1 GHz and 92.6 dBHz$^{2/3}$ at 10 GHz. The performance demonstrated by the thin-film modulators is on par with conventional lithium niobate modulators but with lower drive voltages, smaller device footprints, and potential compatibility for integration with large-scale silicon photonics.** 

***OCIS codes:*** (130.4110) Modulators; (130.3730) Lithium niobate; (250.3140) Integrated optoelectronic circuits; (250.4110) Modulators.

https://doi.org/10.1364/OL.41.005700

The last decade has seen a pronounced increase of interest in optical interconnects [1,2] and integrated radio frequency (RF) photonics [3,4]. Optical modulation, both digital and analog, is a key function for progress in both of these fields. Optical modulators on silicon (Si) substrates are desirable to leverage compatibility with Si electronics and large-scale integration capabilities of the silicon photonics technology [5]. With this aim in mind, one type of modulator that has been widely pursued is the all-silicon integrated modulator [6,7], on the silicon-on-insulator (SOI) platform, based on the free-carrier plasma dispersion effect [8]. High data transmission rates up to 50 Gb/s have been demonstrated but with low extinctions ratios below 7.1 dB [9–12]. On the other hand, conventional lithium niobate (LN) modulators, traditionally used in RF photonic systems, have demonstrated high-performance analog modulation [13,14]. However, these modulators are bulky and not compatible with silicon substrates and thus not suitable for economical large-scale on-chip integration. The limitations of all-silicon and LN modulators have driven the integration of a handful of different material systems on silicon for optical modulation. Some of these include silicon–organic hybrids [15] and heterogeneously integrated electroabsorption and electro-optic (EO) modulators on silicon [16,17].

Most recently, there has been a spurt of interest in the heterogeneous integration of thin-film LN on silicon substrates [18–24]. Our approach has been to rib load thin films of LN on oxidized silicon with a refractive index-matched dielectric to form submicrometer optical modulators [18–20]. In these works, the related processes developed for low-loss index-matched tantalum pentoxide [25,26] and chalcogenide glass [27], as well as silicon nitride, have been used for rib loading the devices but with limited modulation bandwidths and no characterization of intermodulation linearity. An alternative approach has been to bond thin slabs of LN onto prefabricated Si waveguides [21–24].

The work presented in this Letter establishes the performance of submicrometer LN-on-Si Mach–Zehnder (MZ) modulators as on par with conventional lithium niobate counterparts that are commercially available. The half-wave voltage length product $V_\pi \cdot L$ and device footprint demonstrated in this work are significantly lower than that of conventional LN modulators, with comparable extinction ratios, electrical bandwidth, and intermodulation spurious free dynamic range.

MZ modulators in a push-pull configuration with 8 mm arm lengths were fabricated. Conventional LN MZ modulators typically have 3 cm and longer electrode arms. Similar to our pioneering work on the fabrication issues [18], ion implantation and room temperature bonding are used to transfer 400 nm thick films of $Y$-cut LN onto a 2 μm thick layer of thermally grown silicon dioxide on a Si substrate. This in-house process forms the slab region of the ridge optical waveguide. Rib loading with an index-matched material avoids the

challenges of etching LN. As mentioned, we have previously used tantalum pentoxide [18] and chalcogenide [19] ribs.

In this work, we employ silicon nitride due to the ease of processing. Accordingly, a 0.5 μm thick layer of silicon nitride (SiN) is deposited using plasma-enhanced chemical vapor deposition (PECVD). The SiN is deposited at 750 mTorr pressure and 300°C temperature, using a mixture of 2% silane and nitrogen, flowing at 2000 and 10 sccm, respectively. The low-frequency plasma is driven at 60 W. The refractive index of the thin film of SiN is 1.93 at 1550 nm, measured using a prism-coupler commercial setup. 1.3 μm wide strips of SiN are patterned using electron beam lithography (EBL) to form single-mode optical waveguides at 1550 nm by rib loading the LN thin film. Then, a 2 μm thick layer of benzocyclobutene (BCB) is spun and cured as the top optical cladding. Vias, 5–10 μm wide, are etched through the BCB layer and electroplated with gold. Metal pads 8 to 14 μm wide and 2 μm tall are formed above the vias by gold electroplating to complete the fabrication of the traveling-wave metallic electrodes.

A simulation of the optical TE mode performed in COMSOL is shown in Fig. 1(a). Around 70% of the optical mode is confined in the LN slab region. Compared to reported values of a typical conventional titanium-diffused LN waveguide [28], the optical mode area is reduced by ~24 times, i.e., from about 2 μm by 6 μm (half-intensity widths) [28] in conventional diffused LN waveguides to 0.5 μm by 1 μm in this work.

An important benefit of this increased confinement is a significant reduction in the critical bending radius (<200 μm in our approach [19]) compared to the diffused waveguides (>5 mm [29]). Thus, there is negligible optical loss induced in the gentle bends used to form the $Y$-junctions of the MZ modulators. Additionally, the EBL patterning of the waveguides ensures that the tips of the $Y$-junctions are defined very sharply, thereby avoiding any loss at the junctions. The submicrometer waveguides on LN afford a lower $V_\pi \cdot L$ due to the increased optical confinement and good optical–RF field overlap, leading to lower drive voltages and smaller device lengths compared to conventional LN modulators.

The highest EO coefficient of LN, $r_{33} = 31$ pm/V, is utilized by aligning the $z$ axis of the LN crystal along the horizontal RF electric field created by push-pull coplanar waveguide (CPW) traveling wave electrodes. The high-speed performance of traveling wave electrode modulators depends on matching the characteristic impedance of the CPW electrode at radio frequencies to that of the source and load (50 Ω) while minimizing both the velocity mismatch between the optical and RF waves and the loss of the RF wave [30–32].

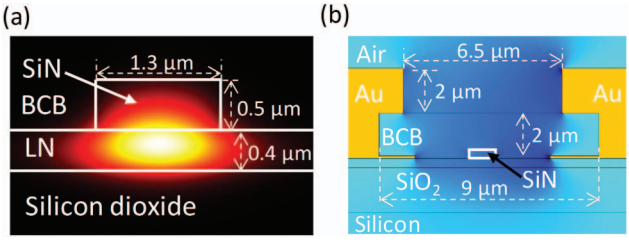


**Fig. 1.** Design dimensions and mode profile simulations using COMSOL for (a) optical TE field at 1550 nm and (b) RF field at 10 GHz.

Thus, the CPW electrodes are designed to maintain a characteristic impedance as close as possible to 50 Ω. The simulations for the electric field characteristics of the CPW electrodes are carried out in COMSOL at radio frequencies ranging from 1 GHz to 10 GHz. The characteristic complex impedance $Z$ of a CPW electrode at a particular radio frequency $\omega$ follows that of a conventional CPW transmission line. Thus, $Z$ is composed of resistive ($R$), inductive ($L$), conductive ($G$), and capacitive ($C$) elements, all per unit length, often referred to as the RLGC model for a transmission line [33]. Each of these components can be further split up and calculated based on different physical regions of the modulator structure. This is particularly important for the more involved capacitances often encountered in silicon optical modulators [34] but is relatively unimportant for this work. The frequency-dependent RLGC transmission line parameters are conveniently derived from the RF electromagnetic field simulations run in COMSOL [33].

The RF-dependent velocity mismatch between the RF and optical waves and the RF propagation loss can both be minimized by appropriate design of the CPW electrodes that balances the three-way tradeoff between velocity mismatch, RF loss, and characteristic impedance for high-speed performance. The RF wave index and propagation loss can be directly extracted from the RF electric field simulations. An additional constraint on the design is that the electrode gap across each waveguide arm of the modulator must be wide enough to not introduce metal induced optical loss, which would increase the on-chip insertion loss and degrade device performance.

An instance of the RF electric field at 10 GHz, simulated in COMSOL, is shown in Fig. 1(b). Similar to conventional LN modulators, the electric field is somewhat sharper at the edge of the electrodes than in the middle of the 5.5 μm wide electrode gap. However, this does not detract from the increase in optical confinement and the decrease of the electrode gap and the subsequent drive voltage reduction, as supported by the $V_\pi \cdot L$ values presented in this work. The reduction in drive voltage could be further enhanced if more of the optical mode is buried in LN than the aforementioned value of 70%. However, this would entail etching the LN, which thus far has not proven to be a viable approach for low loss submicrometer waveguides. Alternatively, the rib loading, as in the structure presented in this work, could be altered to push the optical mode further down into the LN. This would simultaneously result in a decrease in the lateral optical confinement, thus increasing the electrode gap required to avoid metal induced optical loss in the waveguide and thereby defeating the purpose of further lowering the drive power. This tradeoff between lateral optical confinement and the confinement of the mode in the LN ties in with the tradeoffs involved in designing the CPW electrodes through the electrode gap. The particular electrode shape and structure chosen in this work is not a unique solution to balancing these tradeoffs, and more optimized structures can potentially yield improved performance.

Light from a tunable continuous-wave (CW) semiconductor laser was fed through a polarization controller and coupled into and out of the LN-on-Si MZ modulators using end-butt fiber coupling. For low-frequency characterization, a DC coupled photodetector was used to capture the optical response of the modulator. $V_\pi \cdot L$ of 3.1 V.cm and extinction ratio of 18 dB were measured at 1550 nm, as presented in Fig. 2.

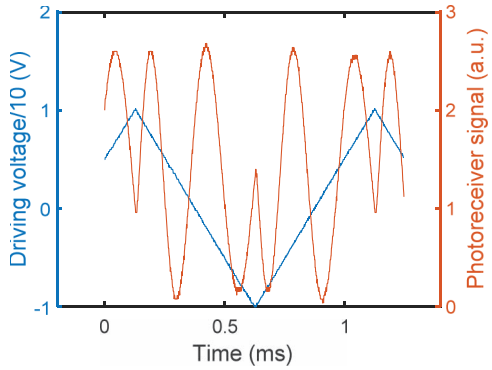


**Fig. 2.** Low-frequency modulation response, demonstrating a $V_\pi \cdot L$ of 3.1 V.cm and extinction ratio of 18 dB.

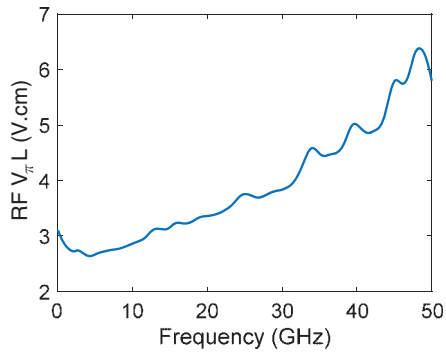


**Fig. 4.** RF $V_\pi \cdot L$, extracted from the measurements shown in Figs. 2 and 3, is less than 6.5 V.cm up to 50 GHz.

To obtain the high-frequency response of the modulator, the electro-optic $S$ parameter ($EO\ S_{21}$) of the MZ modulator was measured from 10 MHz to 50 GHz. A ground–signal–ground (GSG) probe was used to launch the RF signal onto the carefully designed and fabricated coplanar traveling wave electrodes, which were terminated using a standard 50 Ω impedance. One port of a 50 GHz vector network analyzer (VNA) was used as the electrical signal source. A bias tee was used to set the modulator at quadrature. The modulated optical output was fed through an erbium-doped fiber amplifier to a 70 GHz bandwidth high-speed photodiode, which was connected to the second port of the VNA. The VNA was calibrated using short-open-load-thru (SOLT) standards. The electrical return loss ($S_{11}$) is below 10 dB up to 50 GHz and the electrical transmission ($S_{21}$) is smooth up to 50 GHz. The electrical EO bandwidth of the MZ modulator is 33 GHz, as shown in Fig. 3. The $EO\ S_{21}$ has a slight peak near 5 GHz, similar to behavior observed in some conventional LN modulators [35], and remains reasonably flat up to 50 GHz with an electrical roll-off of ∼6 dB, indicating the potential for operation beyond 50 GHz. As plotted in Fig. 4, the RF $V_\pi \cdot L$ was extracted from the measured low frequency $V_\pi \cdot L$ and $EO\ S_{21}$ [36], and evidently it is below 6.5 V.cm up to 50 GHz.

The third-order intermodulation distortion (IMD3) spurious free dynamic range (SFDR) was measured to quantify the linearity of the LN-on-Si MZ modulators biased at quadrature from 1 GHz to 10 GHz. Two RF tones, separated by 10 MHz, were combined and launched using a GSG probe onto the MZ modulator electrodes. The modulated optical output was fed to a 20 GHz bandwidth photodiode, which was connected to a 26 GHz RF spectrum analyzer (RFSA). The results are summarized in Fig. 5. The noise floor of the RFSA varies from −149 dBm/Hz at 1 GHz to −145 dBm/Hz at 10 GHz. The measured IMD3 SFDR is 97.3 $dBHz^{2/3}$ at 1 GHz, 96.6 $dBHz^{2/3}$ at 5 GHz, 93.6 $dBHz^{2/3}$ at 8 GHz, and 92.6 $dBHz^{2/3}$ at 10 GHz. The decrease in the SFDR at higher frequencies is partly due to the degradation of the RFSA noise floor. The SFDR was measured with less than 1 mW of optical power in the modulator. Previously, SFDR values above 110 $dBHz^{2/3}$ have been reported in prior work on conventional LN modulators [37–39]. These have typically relied on higher optical powers and lower RFSA noise floors, around −160 dBm/$Hz$ or lower, leading to higher SFDR. In contrast, the overall SFDR in this work was limited by the noise floor specification of the RFSA used, which was above −150 dBm/Hz. Increasing the optical power in the modulator

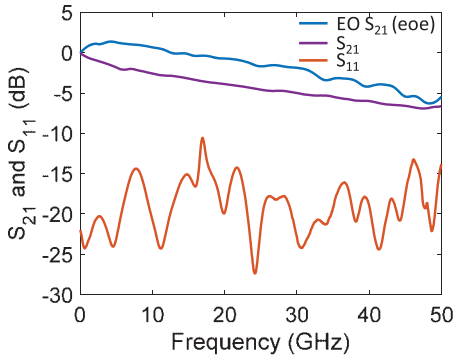


**Fig. 3.** Measured $S$ parameters of the MZ modulators, namely, electrical transmission and reflection ($S_{21}$ and $S_{11}$) and electro-optic transmission ($EO\ S_{21}$). The (eoe) signifies that the electro-optic response $EO\ S_{21}$ is electrical. Evidently, the 3 dB electrical EO bandwidth of the devices is 33 GHz.

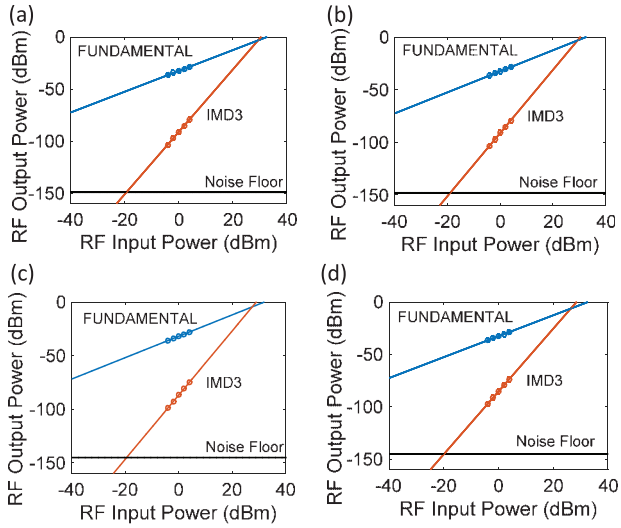


**Fig. 5.** Third-order intermodulation distortion spurious free dynamic range: (a) 97.3 $dBHz^{2/3}$ at 1 GHz, (b) 96.6 $dBHz^{2/3}$ at 5 GHz, (c) 93.6 $dBHz^{2/3}$ at 8 GHz, and (d) 92.6 $dBHz^{2/3}$ at 10 GHz.

and using a different RFSA with a lower noise floor would potentially lead to higher SFDR.

In summary, high-performance LN-on-Si compact modulators have been demonstrated for optical interconnect and RF photonic applications. The results showcase the coming-of-age of thin-film lithium niobate modulators, demonstrating performance on par with commercial lithium niobate modulators but with lower drive voltages, smaller device footprints, and potential compatibility with silicon photonics. The operating range of 50 GHz and the reported spurious free dynamic range values are both limited by the equipment available for characterization and can be further improved.

**Funding.** Office of Naval Research (ONR); U.S. Department of Energy (DOE).

**Acknowledgment.** We thank E. Soto for assistance with characterization.

## REFERENCES

1. D. Miller, Proc. IEEE **97**, 1166 (2009).
2. M. J. R. Heck, H. W. Chen, A. W. Fang, B. R. Koch, D. Liang, H. Park, M. N. Sysak, and J. E. Bowers, IEEE J. Sel. Top. Quantum Electron. **17**, 333 (2011).
3. R. Williamson and R. Esman, J. Lightwave Technol. **26**, 1145 (2008).
4. L. Johansson, S. Estrella, J. Thomas, J. Campbell, D. Renner, and M. Masanovic, Proc. SPIE **9836**, 98360D (2016).
5. B. Jalali and S. Fathpour, J. Lightwave Technol. **24**, 4600 (2006).
6. G. T. Reed, G. Mashanovich, F. Y. Gardes, and D. J. Thomson, Nat. Photonics **4**, 518 (2010).
7. G. T. Reed, G. Z. Mashanovich, F. Y. Gardes, M. Nedeljkovic, Y. Hu, D. J. Thomson, K. Li, P. R. Wilson, S. Chen, and S. S. Hsu, Nanophotonics **3**, 229 (2014).
8. R. A. Soref and B. R. Bennett, IEEE J. Quantum Electron. **23**, 123 (1987).
9. P. Dong, L. Chen, and Y. Chen, Opt. Express **20**, 6163 (2012).
10. T. Baba, S. Akiyama, M. Imai, N. Hirayama, H. Takahashi, Y. Noguchi, T. Horikawa, and T. Usuki, Opt. Express **21**, 11869 (2013).
11. X. Tu, T. Liow, J. Song, X. Luo, Q. Fang, M. Yu, and G. Lo, Opt. Express **21**, 12776 (2013).
12. Y. Yang, Q. Fang, M. Yu, X. Tu, R. Rusli, and G. Lo, Opt. Express **22**, 29978 (2014).
13. K. Noguchi, O. Mitomi, and H. Miyazawa, J. Lightwave Technol. **16**, 615 (1998).
14. J. Macario, P. Yao, S. Shi, A. Zablocki, C. Harrity, R. Martin, C. Schuetz, and D. Prather, Opt. Express **20**, 23623 (2012).
15. M. Lauermann, S. Wolf, P. C. Schindler, R. Palmer, S. Koeber, D. Korn, L. Alloatti, T. Wahlbrink, J. Bolten, M. Waldow, M. Koenigsmann, M. Kohler, D. Malsam, D. L. Elder, P. V. Johnston, N. Phillips-Sylvain, P. A. Sullivan, L. R. Dalton, J. Leuthold, W. Freude, and C. Koos, J. Lightwave Technol. **33**, 1210 (2015).
16. S. Fathpour, Nanophotonics **4**, 143 (2015).
17. T. Komljenovic, M. Davenport, J. Hulme, A. Liu, C. Santis, A. Spott, S. Srinivasan, E. Stanton, C. Zhang, and J. E. Bowers, J. Lightwave Technol. **34**, 20 (2016).
18. P. Rabiei, J. Ma, S. Khan, J. Chiles, and S. Fathpour, Opt. Express **21**, 25573 (2013).
19. A. Rao, A. Patil, J. Chiles, M. Malinowski, S. Novak, K. Richardson, P. Rabiei, and S. Fathpour, Opt. Express **23**, 22746 (2015).
20. A. Rao, A. Patil, J. Chiles, M. Malinowski, S. Novak, K. Richardson, P. Rabiei, and S. Fathpour, in *Conference on Laser and Electro-Optics*, OSA Technical Digest (online) (Optical Society of America, 2015), paper STu2F.4.
21. Y. S. Lee, G. D. Kim, W. J. Kim, S. S. Lee, W. G. Lee, and W. H. Steier, Opt. Lett. **36**, 1119 (2011).
22. L. Chen, Q. Xu, M. Wood, and R. Reano, Optica **1**, 112 (2014).
23. A. Mercante, P. Yao, S. Shi, G. T. Schneider, J. Murakowski, and D. Prather, Opt. Express **24**, 15590 (2016).
24. P. O. Weigel, M. Savanier, C. T. DeRose, A. T. Pomerene, A. L. Starbuck, A. L. Lentine, V. Stenger, and S. Mookherjea, Sci. Rep. **6**, 22301 (2016).
25. P. Rabiei, J. Ma, S. Khan, J. Chiles, and S. Fathpour, Opt. Express **21**, 6967 (2013).
26. P. Rabiei, A. Rao, J. Chiles, J. Ma, and S. Fathpour, Opt. Lett. **39**, 5379 (2014).
27. J. Chiles, M. Malinowski, A. Rao, S. Novak, K. Richardson, and S. Fathpour, Appl. Phys. Lett. **106**, 111110 (2015).
28. M. Fukuma and J. Noda, Appl. Opt. **19**, 591 (1980).
29. R. F. Tavlykaev, K. Kueckelhaus, and E. I. Voges, Proc. SPIE **2150**, 263 (1994).
30. R. C. Alferness, S. K. Korotky, and E. A. J. Marcatili, IEEE J. Quantum Electron. **20**, 301 (1984).
31. A. Chowdhury and L. McCaughan, Opt. Lett. **26**, 1317 (2001).
32. J. A. I. Fuste and M. C. S. Blanco, Opt. Lett. **38**, 1548 (2013).
33. D. M. Pozar, *Microwave Engineering* (Wiley, 1998).
34. J. Wang, C. Qiu, H. Li, W. Ling, L. Li, A. Pang, Z. Sheng, A. Wu, X. Wang, S. Zou, and F. Gan, J. Lightwave Technol. **31**, 4119 (2013).
35. E. L. Wooten, K. M. Kissa, A. Yi-Yan, E. J. Murphy, D. A. Lafaw, P. F. Hallemeier, D. Maack, D. V. Attanasio, D. J. Fritz, G. J. McBrien, and D. E. Bossi, IEEE J. Sel. Top. Quantum Electron. **6**, 69 (2000).
36. W. S. Chang, *RF Photonic Technology in Optical Fiber Links* (Cambridge University, 2002).
37. B. Kolner and D. Dolfi, Appl. Opt. **26**, 3676 (1987).
38. E. Ackerman, S. Wanuga, D. Kasemset, A. S. Daryoush, and N. R. Samant, IEEE Trans. Microw. Theory Tech. **41**, 1299 (1993).
39. J. H. Schaffner, J. F. Lam, C. J. Gaeta, G. L. Tangonan, R. L. Joyce, M. L. Farwell, and W. S. C. Chang, IEEE Photon. Technol. Lett. **6**, 273 (1994).